

High-accuracy estimation of magnetic field strength in the interstellar medium from dust polarization

Raphael Skalidis and Konstantinos Tassis

¹ Institute of Astrophysics, Foundation for Research and Technology-Hellas, Vasilika Vouton, GR-70013 Heraklion, Greece
e-mail: rskalidis@physics.uoc.gr,

² Department of Physics & ITCP, University of Crete, GR-70013, Heraklion, Greece
e-mail: tassis@physics.uoc.gr

ABSTRACT

Context. A large-scale magnetic field permeates our Galaxy and is involved in a variety of astrophysical processes such as star formation and cosmic ray propagation. Dust polarization has been proven one of the most powerful observables for studying the field properties in the interstellar medium (ISM). However, it does not provide a direct measurement of its strength. Different methods have been developed which employ both polarization and spectroscopic data in order to infer the field strength. The most widely applied methods have been developed by [Davis \(1951\)](#), [Chandrasekhar & Fermi \(1953\)](#) (DCF), [Hildebrand et al. \(2009\)](#) and [Houde et al. \(2009\)](#) (HH09). They rely on the assumption that isotropic turbulent motions initiate the propagation of Alfvén waves. Observations, however, indicate that turbulence in the ISM is anisotropic and non-Alfvénic (compressible) modes may be important.

Aims. Our goal is to develop a new method for estimating the field strength in the ISM, which includes the compressible modes and does not contradict the anisotropic properties of turbulence.

Methods. We adopt the following assumptions: 1) gas is perfectly attached to the field lines; 2) field line perturbations propagate in the form of small-amplitude MHD waves; 3) turbulent kinetic energy is equal to the fluctuating magnetic energy. We use simple energetics arguments that take into account the compressible modes to estimate the strength of the magnetic field.

Results. We derive the following equation: $B_0 = \sqrt{2\pi\rho\delta v}/\sqrt{\delta\theta}$, where ρ is the gas density, δv is the rms velocity as derived from the spread of emission lines, and $\delta\theta$ is the dispersion of polarization angles. We produce synthetic observations from 3D MHD simulations and we assess the accuracy of our method by comparing the true field strength with the estimates derived from our equation. We find a mean relative deviation of 17%. The accuracy of our method does not depend on the turbulence properties of the simulated model. In contrast DCF and HH09 systematically overestimate the field strength. HH09 produces accurate results only for simulations with high sonic Mach numbers.

Conclusions. Compressible modes can affect significantly the accuracy of methods that are based solely on Alfvénic modes. The formula that we propose includes compressible modes; however it is applicable only in regions with no self-gravity. Density inhomogeneities may bias our estimates to lower values.

Key words. magnetic field – interstellar medium (ISM) – dust polarization

1. Introduction

The Galactic magnetic field plays a key role in various astrophysical processes, such as cosmic ray propagation and star formation, and affects foregrounds relevant to cosmic microwave background polarization experiments. Various tracers exist revealing either the line of sight (LOS) or the plane of the sky (POS) component of the field. Zeeman splitting is sensitive to the LOS component and is the only observable, which reveals both the local magnitude and the direction of the field vector. Regarding the POS component, synchrotron and dust polarization are the most common observables. Unlike synchrotron, dust polarization traces the POS field in the cold neutral medium, where stars form. Dust polarization reveals only the morphology of the field and not its strength (see [Andersson et al. 2015](#), for a recent review). Different magnetic field strength estimation methods have been developed using the dust polarization data.

The first method was presented by [Davis \(1951\)](#) and [Chandrasekhar & Fermi \(1953\)](#) (DCF). They assumed that magnetic field lines are distorted due to the propagation of the incompressible transverse magnetohydrodynamic (MHD) waves, known as Alfvén waves. This distortion induces spread in the polarization

angle distribution, which, combined with the gas turbulent motions from spectroscopic data, allows the estimate of the true magnetic field strength. Different effects have been recognized to bias the accuracy of the DCF method towards higher values ([Zweibel 1990](#); [Myers & Goodman 1991](#)). [Ostriker et al. \(2001\)](#), [Padoan et al. \(2001\)](#), and [Heitsch et al. \(2001\)](#), after testing the accuracy of the method in MHD simulations, found that on average the method produces a two-fold deviation. In addition, it was realized that external forces, like self-gravity, can bend the field lines and induce extra dispersion in the polarization angle distribution. In order to treat the problem, [Girart et al. \(2006\)](#) fitted parabolas to the polarization data and removed the large-scale hour-glass bending from the polarization data of a pre-stellar core. A similar, but more sophisticated approach, was followed by [Pattle et al. \(2017\)](#). On the other hand, [Hildebrand et al. \(2009\)](#) and [Houde et al. \(2009\)](#) (HH09) developed an analytical model for the polarization data, which measures the turbulence-induced spread in the presence of any external source of B-field bending. Other modifications of the DCF method have also been developed ([Heitsch et al. 2001](#); [Kudoh & Basu 2003](#); [Falceta-Gonçalves et al. 2008](#); [Cho & Yoo 2016](#); [Yoon & Cho 2019](#);

Lazarian et al. 2020). See Pattle & Fissel (2019) and Hull & Zhang (2019) for recent reviews. All these methods rely on the assumption that the Alfvén waves are producing the observed polarization angle dispersion and the linewidths in the emission spectra.

The interstellar medium (ISM) is highly compressible and other than the Alfvén waves, contains MHD wave modes that induce density compressions. These are known as fast and slow magnetosonic modes and their existence in astrophysical plasmas is inevitable because they are excited by the Alfvén waves, e.g. Heyvaerts & Priest (1983). In addition, the so-called entropy modes can contribute to the observed compressibility of the ISM (Lithwick & Goldreich 2001), however they produce zero velocity and magnetic field fluctuations. All the aforementioned methods ignore the existence of the compressible modes. This can lead to significant inaccuracies in the magnetic field strength estimates.

In the present work, we propose a new relation for estimating the field strength, which, unlike the DCF and HH09 methods, *includes the compressible modes*. We assess the validity of this method in synthetic observations that we produce from 3D MHD turbulence simulations. Our method employs both polarization and spectroscopic data. Its applicability should be restricted to regions that do not show large-scale bending due to self-gravity.

The structure of the paper is as follows. In Section 2 we critically review the DCF method. We review the underline assumptions and point out projection effects that may affect its accuracy. We test the method in 3D simulations. In Section 3 we critically review the HH09 method and we apply it in synthetic observations of 3D simulations. In Section 4 we present our new method and apply it in 3D simulations and discuss its limitations. In Section 5 we summarize our results.

2. Classical DCF method

2.1. Foundations of the method

We decompose the total magnetic field into a mean, \mathbf{B}_0 , and a fluctuating component $\delta\mathbf{B}$. The total field is $\mathbf{B} = \mathbf{B}_0 + \delta\mathbf{B}$ with a total magnetic energy density equal to

$$\frac{B^2}{8\pi} = \frac{1}{8\pi} [B_0^2 + \delta B^2 + 2\delta\mathbf{B} \cdot \mathbf{B}_0], \quad (1)$$

where bold letters are used to denote vectors. The last two terms correspond to changes of the magnetic energy, $\delta\epsilon_m$, due to $\delta\mathbf{B}$ fluctuations. DCF assumed that the ISM plasma conductivity is infinite. This means that the magnetic field is "frozen-in" the gas, hence both gas and field lines oscillate in phase. Turbulent gas motions perturb the field lines and initiate small amplitude fluctuations, $|\delta\mathbf{B}| \ll |\mathbf{B}_0|$, in the form of Alfvén waves about the mean field. DCF assumed that the kinetic energy of turbulent motions will be equal to the fluctuating magnetic energy density

$$\frac{1}{2}\rho\delta v^2 = \frac{\delta B^2}{8\pi}, \quad (2)$$

where ρ is the gas density and δv the rms velocity. Note that $\mathbf{B}_0 \cdot \delta\mathbf{B} = 0$, since Alfvén waves are transverse. We divide both sides by B_0^2 and after rearranging we obtain

$$B_0 = \sqrt{4\pi\rho\delta v} \left[\frac{\delta B}{B_0} \right]^{-1}. \quad (3)$$

The magnetic field orientation is traced by dust polarization (with a π ambiguity) and the dispersion of the polarization angle distribution, $\delta\theta$, is a metric of $\delta B/B_0$. If the mean field is

stronger than the fluctuating component, the field lines will appear approximately straight, hence $\delta\theta$ will be small. If, on the other hand, the fluctuations are relatively large, field lines will be dispersed by turbulent motions and $\delta\theta$ will increase. Thus, DCF assumed $\delta\theta = \delta B/B_0$, yielding

$$B_0 = \sqrt{\frac{4\pi\rho}{3}} \frac{\delta v}{\delta\theta}, \quad (4)$$

where the factor $1/\sqrt{3}$ was inserted by DCF because they assumed that turbulent motions are isotropic and only one of the three Cartesian velocity components perturbs the field lines. Other authors (see Ostriker et al. 2001) proposed a different correction factor f . The generalized DCF equation is then

$$B_0 = f \sqrt{4\pi\rho} \frac{\delta v}{\delta\theta}. \quad (5)$$

The mean magnetic field, B_0 , can be written in velocity units by dividing by $\sqrt{4\pi\rho}$, thus

$$V_A = f \frac{\delta v}{\delta\theta}, \quad (6)$$

where V_A is the Alfvén speed.

2.2. Caveats of the method

2.2.1. Turbulent velocities and compressible modes

The DCF method has been used extensively in atomic and molecular clouds. Turbulent velocities, denoted as δv or σ_v , are measured using spectroscopic data, e.g. H_I 21cm line, CO(J=1-0) line, etc. Emission lines are approximated as Gaussians and non-thermal linewidths are usually observed. The non-thermal broadening, $\sigma_{v,turb}$, is attributed to turbulent gas motions, so

$$\sigma_{v,turb}^2 = \sigma_{v,tot}^2 - \sigma_{v,thermal}^2, \quad (7)$$

where $\sigma_{v,tot}$ is the total observed spread and $\sigma_{v,thermal}$ the thermal broadening. Note that in many works, e.g. Panopoulou et al. (2016), the FWHM is used instead of $\sigma_{v,turb}$. We find the latter more appropriate, since it is directly connected with the velocity rms.

Turbulent broadening, $\sigma_{v,turb}$, may contain contributions from wave modes other than the Alfvén modes. MHD plasma also supports the propagation of fast and slow modes, which can be excited even if they are not initially in the system (Heyvaerts & Priest 1983), due to their coupling with Alfvén modes. These modes can induce extra dispersion in the observed velocities and significantly affect the DCF method, which neglects their contribution.

The ISM is highly compressible (e.g., Heiles & Troland 2003). This implies that $\sigma_{v,turb}$ includes velocities from both Alfvén and compressible modes. As a result, $\sigma_{v,turb}$ will always be higher than by Alfvén waves alone, hence B_0 will be overestimated. This makes the mode decomposition necessary in order to apply the DCF method accurately. However, mode decomposition is not trivial in observations.

2.2.2. Projection effects and the polarization angle distribution

Similar to velocities, fast and slow modes can also induce $\delta B/B$ variations (Cho & Lazarian 2002). As a result, non-Alfvénic modes will contribute to the observed signal, which will be larger

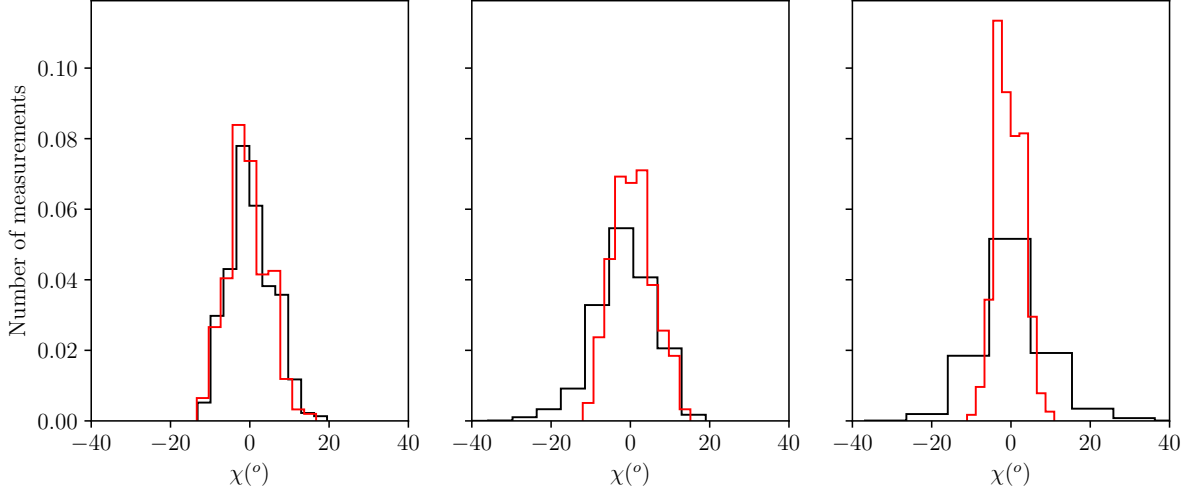


Fig. 1. Distribution of the synthetic polarization angles for different simulation models. Black histogram corresponds to observations weighted by density, while the red one without the density weighting. **Left:** Simulation model with $M_s = 0.7$, **Middle:** Simulation model with $M_s = 2.0$, **Right:** Simulation model with $M_s = 7.0$.

than the Alfvénic. Observationaly $\delta B/B_0$ is computed from the spread in the polarization angle distribution, $\delta\theta$. However, $\delta\theta$ may not trace $\delta B/B_0$ accurately. We present two projection effects that are related to this discrepancy. The first one has been demonstrated in previous works, while to our knowledge we are the first to demonstrate the second.

1. Degeneracy with the LOS angle

According to equation (5), B_0 is inversely proportional to $\delta\theta$. This means that regions with highly disordered magnetic field, i.e. high $\delta\theta$, have a weak field strength. However, high $\delta\theta$ can also be obtained if the magnetic field is mostly parallel to the LOS. In this case, even small perturbations will lead to POS fields that look highly disordered (Ostriker et al. 2001; Falceta-Gonçalves et al. 2008; Hensley et al. 2019). Thus, there is a degeneracy in $\delta\theta$ between the viewing angle of the magnetic field and the field strength (Ostriker et al. 2001; Falceta-Gonçalves et al. 2008).

2. Non-homogeneity effect

Zweibel (1990) and Myers & Goodman (1991) proposed that the dispersion of the polarization angles, $\delta\theta$, is systematically lower due to line of sight averaging of the magnetic field directions. They argued that the polarization signal is averaged over N distinct, independent regions (turbulent cells) along the LOS. Thus, $\delta\theta$ is biased towards lower values, and the magnetic field strength is systematically overestimated.

Consider, however, a Cartesian coordinate system with (discrete) independent variables i, j, k . The ij plane is the POS and k is parallel to the LOS. The Stokes parameters are (Lee & Draine 1985),

$$I_{ij} = \sum_{k=1}^L \rho_{ijk}, \quad (8)$$

$$Q_{ij} = \sum_{k=1}^L \rho_{ijk} \frac{(B_{ijk}^i)^2 - (B_{ijk}^j)^2}{B_{ijk}^2}, \quad (9)$$

$$U_{ij} = \sum_{k=1}^L 2\rho_{ijk} \frac{B_{ijk}^i B_{ijk}^j}{B_{ijk}^2}, \quad (10)$$

where L is the LOS dimension of the cloud, ρ_{ijk} the volume density of the gas, B_{ijk}^i, B_{ijk}^j are the i and j component of the magnetic field respectively, and B_{ijk}^2 the square of the total field strength. The polarization angle is

$$\chi = 0.5 \arctan(U/Q). \quad (11)$$

Since the Stokes parameters are averages with density weights, density variations along the LOS may increase $\delta\theta$. We produce synthetic observations of 3D simulations in order to demonstrate this effect.

We use the publicly available simulations from the CATS database¹ (Burkhart et al. 2020), from which we extract the "Cho-ENO" models (Cho & Lazarian 2003; Burkhart et al. 2009; Portillo et al. 2018; Bialy & Burkhart 2020). These simulations solve the ideal MHD equations using an isothermal equation of state in a box with periodic boundary conditions and no self-gravity. Turbulence is driven solenoidally. The simulations are scale-free in dimensionless units with the dimensionless sound speed, \tilde{c}_s , regulating the units. We convert to cgs units following Hill et al. (2008) and we adopt a sound speed $c_{s,obs} = 0.91$ km/s, which is typical of H_I clouds at $T = 100$ K. All the models have Alfvén Mach number, defined as $M_A = \delta v/V_A$, equal to 0.7, while the sonic Mach number, $M_s = \delta v/\tilde{c}_s$, ranges from 0.7 - 7.0. We use models with $M_A = 0.7$ only, in order to match observations, which indicate that the ISM turbulence is sub/trans-Alfvénic, see § 2.2.3 below.

We create synthetic polarization maps for every simulation model by computing the Stokes parameters and the polarization angles with equations (8)-(11). The dispersion of the polarization angles, $\delta\theta$, for each model is shown in Table 1 in column 4.

In Fig. 1 we show the polarization angle distributions from three different simulation setups with $M_s = 0.7$ (left panel), $M_s = 2.0$ (middle panel), $M_s = 7.0$ (right panel). The black histogram corresponds to the polarization angles computed using equation (11). The red histograms correspond to the distribution of polarization angles when we integrate by setting $\rho = 1$ everywhere in the box. Histograms are normalized so that the

¹ <https://www.mhd turbulence.com/>

area under each histogram integrates to one. The un-weighted distributions become narrower at larger M_s , because more independent turbulent cells are created along the LOS. On the other hand, the density-weighted distributions (black) become wider, because more significant overdensities are created due to enhanced compression at larger M_s . It appears that density fluctuations can induce extra dispersion in the observed polarization angle distribution. Thus, in contrast to Zweibel (1990) and Myers & Goodman (1991), we have found that the LOS averaging of the polarization angles can induce extra dispersion and as a result the magnetic field strength is systematically underestimated.

2.2.3. Different f values

Chandrasekhar & Fermi (1953) assumed that *turbulent motions are isotropic* and they adopted $f = 1/\sqrt{3}$. If the field strength is weak, turbulent motions will drag the field lines towards random directions and turbulence will be isotropic (super-Alfvénic turbulence). However, there is overwhelming observational evidence that magnetic fields in the ISM have well-defined directions indicating that turbulence is sub/trans-Alfvénic, and hence turbulent properties are highly anisotropic (see for example, Montgomery & Turner 1981; Shebalin et al. 1983; Higdon 1984; Sridhar & Goldreich 1994; Goldreich & Sridhar 1995, 1997). Heyer et al. (2008) using CO data, found that velocity structures in Taurus are highly anisotropic. In the same region, Goldsmith et al. (2008) reported the existence of highly-anisotropic density structures, which are aligned parallel to the mean field, known as striations. Striations have also been observed in the Polaris Flare (Panopoulou et al. 2015) and Musca (Cox et al. 2016; Tritsis & Tassis 2018) and they are formed due to magnetosonic waves (Tritsis & Tassis 2016) in sub-Alfvénic turbulence (Beattie & Federrath 2020). More evidence for ordered magnetic fields in molecular clouds can be found in Franco et al. (2010), Franco & Alves (2015), Pillai et al. (2015), Hoq et al. (2017), and Tang et al. (2019). Stephens et al. (2011) explored the magnetic field properties of 52 star forming regions in our Galaxy and concluded that more than 80% of their targets exhibit ordered magnetic fields. The diffuse atomic clouds in our Galaxy are preferentially aligned with the magnetic field (Clark et al. 2014) implying the importance of the magnetic field in their formation. Planck Collaboration et al. (2016) studied a larger sample of molecular clouds in the Goult Belt and concluded that density structures align parallel or perpendicular to the local mean field direction. This is also consistent with sub/trans-Alfvénic turbulence, e.g. Soler et al. (2013). In addition, Mouschovias et al. (2006), using Zeeman data, concluded that turbulence in molecular clouds is slightly sub-Alfvénic as well. All these lines of evidence indicate that ISM turbulence is sub/trans-Alfvénic, and hence anisotropic.

Other f values were proposed when the DCF method was applied in numerical simulations. Ostriker et al. (2001) performed MHD numerical simulations of giant molecular clouds. They produced synthetic observations and suggested that the DCF equation with $f = 0.5$ produces accurate measurements for their sub-Alfvénic model. Padoan et al. (2001) simulated protostellar cores and tested the DCF equation in three different cores in a super-Alfvénic MHD turbulent box. They varied the position of the observer with respect to the magnetic field direction and found that on average $f = 0.4$. However, note that their values range from 0.29 up to 0.74 (see their Table 1). Heitsch et al. (2001) performed 3D MHD simulations of molecular clouds. They found that f lies in the interval 0.33 – 0.5 (see their Fig-

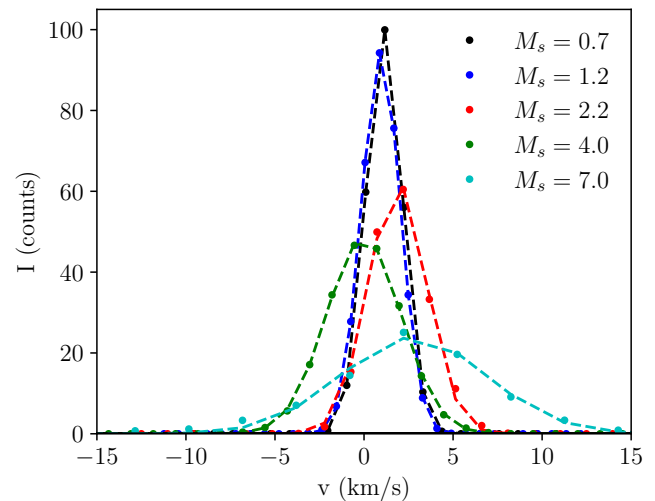


Fig. 2. Synthetic emission line profiles for different simulation models. All the models have Alfvén Mach number $M_A = 0.7$. The sonic Mach number, M_s , for each simulation model is shown in the legend. The dashed lines correspond to the fitted Gaussian profiles.

ure 6) in their three models with strong magnetic fields (sub-Alfvénic turbulence).

In these works f was found to vary significantly, but a value of $f = 0.5$ is widely used, e.g. Pattle & Fissel (2019). However, no physical connection of f with the turbulent properties of the medium or with specific LOS averaging effects has been demonstrated. Thus, it remains unclear, which value of f is most appropriate for any given real physical cloud.

2.3. Testing classical DCF with 3D simulations

We test the DCF method with $f = 0.5$ in the 3D numerical simulation we used in Section 2.2.2. We create synthetic spectroscopic data following Miville-Deschénes et al. (2003), who assumed optically thin emission and included no chemistry. We set the LOS parallel to the z -axis. We compute the PPV cube, $I(x, y, v)$, along the LOS using the following equation,

$$I(x, y, v) = \sum_z \frac{\rho(x, y, z) \delta z}{\sqrt{2\pi}\sigma(x, y, z)} \exp\left[-\frac{(v_{los}(x, y, z) - v)^2}{2\sigma(x, y, z)^2}\right], \quad (12)$$

where $v_{los}(x, y, z)$ is the LOS velocity component, v is the central velocity of each velocity channel and $\delta z = 1$ pixel. The velocity spread is

$$\sigma(x, y, z) = \left[\left(\frac{\partial v_{los}(x, y, z)}{\partial z} \delta z \right)^2 + \frac{k_B T}{m} \right]^{1/2}. \quad (13)$$

In Fig. 2 we show the mean emission profile of each simulation setup derived using equation (12). The dots represent the intensity, I , versus the gas velocity and the dashed lines the fitted Gaussians. From the fitted Gaussians we derive the standard deviation of each profile, shown in the σ_v column of Table 1. In the same Table we show the standard deviation of the polarization angle distribution, $\delta\theta$, for each setup, and the estimated Alfvén speed, using the DCF relation (equation (5) with $f = 0.5$) in the V_A^{DCF} column. The true Alfvén speed for each setup is shown in the column V_A^{true} .

The DCF method systematically overestimates the magnetic field strength. For models with $M_s = 0.7$ and 1.2 DCF without

Table 1. 3D MHD simulation

M_s	V_A^{true}	σ_v	$\delta\theta$	V_A^{DCF}	$\langle B_t^2 \rangle^{0.5} / B_0$	V_A^{HH09}	V_A^{new}
0.7	0.91	0.46	0.097	2.3	0.088	5.2	1.0
1.2	1.60	0.58	0.116	2.4	0.129	4.5	1.2
2.0	2.87	1.36	0.128	5.2	0.212	6.3	2.7
4.0	5.09	1.89	0.132	7.1	0.340	5.5	3.7
7.0	9.10	3.98	0.146	13.5	0.473	8.4	7.4

Notes. The following columns are measured in units of km/s: V_A^{true} , σ_v , V_A^{DCF} , V_A^{HH09} and V_A^{new} . The quantities $\delta\theta$ and $\sqrt{\langle B_t^2 \rangle} / B_0$ are measured in radians.

an f factor ($f = 1$) deviates from the true value by a factor of ~ 5 . This implies that $f = 1/5$ in order for the method to produce accurate estimates. On the other hand, for models with $M_s = 4.0$ and 7.0 the correction factor has to be $f \sim 1/3$. It is evident that the generally adopted $f = 0.5$ value does not apply for these models. Our results indicate that f decreases with M_s , but it remains to be shown whether and why this can be considered a general property.

3. HH09 method

3.1. Foundations of the method

One widely accepted modification of the classical DCF method has been presented by Hildebrand et al. (2009) and Houde et al. (2009), here HH09. The method was developed in order to avoid inaccurate estimates of the magnetic field strength induced by sources other than MHD waves, e.g. large-scale bending of the magnetic field due to gravity and differential rotation. HH09 computed the *isotropic structure function* of the polarization map, following the definition by Falceta-Gonçalves et al. (2008), as

$$\langle [\Delta\Phi^2(l)]^{1/2} \rangle = \sqrt{\frac{1}{N(l)} \sum_{i=1}^{N(l)} [\Phi(\mathbf{x}) - \Phi(\mathbf{x} + \mathbf{l})]^2}. \quad (14)$$

The quantity $\Phi(\mathbf{x})$ denotes the polarization angle measured in degrees, \mathbf{x} denotes the 2D coordinates in the POS, \mathbf{l} the spatial separation of two polarization measurements in the POS and $N(l)$ is the number of measurements separated by a distance l . The averaging is performed over the entire polarization map.

Like DCF, HH09 defined the total magnetic field as $\mathbf{B}_{tot} = \mathbf{B}_0 + \mathbf{B}_t$, where \mathbf{B}_0 is the mean magnetic field component and \mathbf{B}_t the turbulent (or random) component. They assumed that \mathbf{B}_0 is uniform and \mathbf{B}_t is induced by the propagation of Alfvén waves. They derived the following analytical relation for the structure function

$$\langle \Delta\Phi^2(l) \rangle = \frac{\langle B_t^2 \rangle}{B_0^2} + m^2 l^2, \quad (15)$$

where m is a constant. The validity of this relation is limited to spatial scales $\delta \leq l \leq d$, where δ is the correlation length of \mathbf{B}_t and d is the upper limit below which \mathbf{B}_0 remains uniform.

Houde et al. (2009) added the effects of LOS averaging and the resolution of the instrument beam on equation (15). They derived

$$\langle \Delta\Phi^2(l) \rangle \simeq 2 \sqrt{2\pi} \frac{\langle B_t^2 \rangle}{B_0^2} \frac{\delta^3}{(\delta^2 + 2W^2)\Delta'} \times (1 - e^{l^2/2\delta^2}) + ml^2, \quad (16)$$

where Δ' is the depth of the cloud and W the beam size. The above equation is used to estimate the $\langle B_t^2 \rangle^{1/2} / B_0$ term, and then compute the field strength as,

$$V_A^{HH09} \simeq \sigma_v \left[\frac{\langle B_t^2 \rangle^{1/2}}{B_0} \right]^{-1}. \quad (17)$$

Equation (17) is similar to the DCF, equation (6), but instead of $\delta\theta$ they have used $\langle B_t^2 \rangle^{1/2} / B_0$ estimated from the structure function.

In order to use the method, one has to compute the structure function using equation (14), and then fit the model in the right hand side of equation (16). The fit has the following four free parameters: b , W , δ and m , where

$$b^2 = \sqrt{2\pi} \frac{\langle B_t^2 \rangle}{B_0^2} \frac{\delta^3}{(\delta^2 + 2W^2)\Delta'}. \quad (18)$$

For optical polarization measurements, pencil beams are used and $W = 0$ (Franco et al. 2010; Panopoulou et al. 2016), hence the fit reduces to three free parameters.

3.2. Caveats of the method

3.2.1. Omission of compressible modes

Hildebrand et al. (2009) assumed that *the correlation of B_t and B_0 is zero*, i.e. $\langle B_0 \cdot B_t \rangle = 0$, where the averaging is over the full map (see their equation A2). This holds for super-Alfvénic turbulence or for purely Alfvénic turbulence (Goldreich & Sridhar 1995). In super-Alfvénic turbulence, $B_t \gg B_0$, and the correlation of B_t with B_0 is very weak. Thus,

$$\langle \mathbf{B}_t \cdot \mathbf{B}_0 \rangle = \langle \mathbf{B}_0 \rangle \cdot \langle \mathbf{B}_t \rangle = 0 \quad (19)$$

since $\langle \mathbf{B}_t \rangle = 0$. For sub-Alfvénic, but incompressible turbulence, $\mathbf{B}_t \cdot \mathbf{B}_0 = 0$, because Alfvén waves are transverse and their field fluctuations, \mathbf{B}_t , are perpendicular to the mean field \mathbf{B}_0 . The cross-term, $\langle \mathbf{B}_0 \cdot \mathbf{B}_t \rangle$, is connected with the compressible modes (Montgomery et al. 1987), for which $\mathbf{B}_t \cdot \mathbf{B}_0 \neq 0$ (Goldreich & Sridhar 1995). This can be understood, since fast modes are longitudinal and propagate almost isotropically in the medium. Like DCF, compressible modes are not considered, which is in conflict with observational data that reveal ubiquitous supersonic motions.

3.2.2. Isotropic turbulence

HH09 assumed that *turbulence is isotropic* and they used a global correlation length, δ . As we argued in § 2.2.3, this is against observational evidence, which shows highly anisotropic structures and properties. Anisotropic media exhibit different

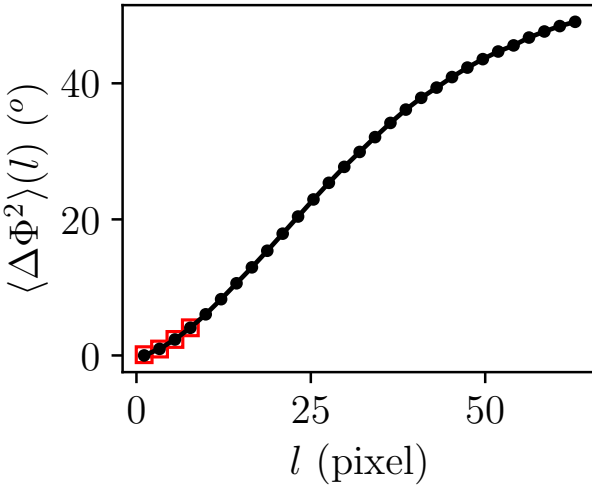


Fig. 3. Structure function for the model with $M_s = 0.7$. The red squares correspond to the model fitted values.

correlation lengths perpendicular and parallel to the mean field. This has been shown in the observations of Higdon (1984) and Heyer et al. (2008) and by numerous theoretical works, e.g. Shebalin et al. (1983), Goldreich & Sridhar (1995), Sridhar & Goldreich (1994), Cho & Vishniac (2000), and Maron & Goldreich (2001) (see Oughton & Matthaeus 2020, for a recent review). This indicates that anisotropic structure functions, similar to Cho & Vishniac (2000) and Maron & Goldreich (2001), should be used instead.

3.2.3. Fitting range of structure function

The HH09 method involves the fitting of the structure function with equation (16), which is valid for $l \rightarrow 0$ (Hildebrand et al. 2009). The $l \rightarrow 0$ approximation has been interpreted differently by various authors. For example, Hildebrand et al. (2009) performed the fit using only 3 points up to scales $\sim 1'$. On the other hand, Panopoulou et al. (2015) used 8 points up to scales $\sim 10'$, while Chuss et al. (2019) used more than 15 points up to scales $\sim 0.5'$. The fit may vary with the number of points used, and so does the estimated magnetic field strength, see for example Appendix A.

3.2.4. Sparsity of data and the structure function

Another problem is related to the structure function computation in sparse data. Soler et al. (2016) showed that the structure function computed with optical polarization is slightly different than the one computed with sub-mm data, see their Fig. 6. They commented that the sparse sampling of the optical polarization measurements induces a "jittering". Their figures indicate that the structure function with the optical data systematically overestimates the intercept of the function. As a result, for the case of the sparse sampling, the b parameter would be biased towards higher values. No solution to this problem has been suggested yet.

3.3. Testing HH09 with 3D simulations

We apply the HH09 method to the polarization angle maps, $\chi(x, y)$, we created in Section 2.2.2. We compute the structure function following equation (14). The polarization angle differences are constrained in the interval $[0^\circ, 90^\circ]$. In Fig. 3 we show in black the computed structure function for the model with $M_s = 0.7$. We fit the model of equation (16) to this function. In our synthetic observations there is no beam effect, hence $W = 0$. Our fit reduces to the following parameters: δ , b and m . From b we solve for $\langle B_t^2 \rangle^{1/2} / B_0$, which is inserted in equation (17) in order to compute the field strength. Note that the structure function is measured in degrees. We convert it to radians, before we use it in equation (17).

HH09 method assume $l \rightarrow 0$ (Hildebrand et al. 2009). In order to be consistent with this approximation we use only the first four points in the fitting of the function in Fig. 3. This allows enough degrees of freedom for the fit. The red squares show the fit of equation (16). We compute the structure function and the $\langle B_t^2 \rangle^{1/2} / B_0$ term for the simulation models with $M_s = 1.2 - 7.0$. The best fit parameters for all models are given in Appendix A.

The turbulent-to-ordered ratio obtained for the different simulation models is shown in column $\langle B_t^2 \rangle^{1/2} / B_0$, in Table 1. The estimated Alfvén speed with the HH09 method is shown in the same Table in the V_A^{HH09} column. The HH09 method in the models with $M_s = 0.7 - 2.2$ overestimates the "true" Alfvén speed (V_A^{true}). The overestimation of the magnetic field value by the HH09 method in these models is more prominent than the DCF method (V_A^{DCF}). This is consistent with the observations, which indicate that the HH09 method produces larger magnetic field values compared to other methods (Pattle & Fissel 2019). We note, however, that in the models with the highest Mach number, $M_s = 4.0$ and 7.0 , the method produces fairly accurate estimates of the field strength. More simulations are necessary in order to verify if this is a general behaviour of the method.

4. Proposed method

Motivated by the existence of compressible modes and the contamination they induce in the aforementioned methods, we propose a generalized method, which takes into account these modes. We start with equation (1). Similar to DCF, we assume that gas is perfectly attached to the magnetic field and that turbulent motions are completely transferred to magnetic fluctuations. Unlike DCF method, we assume that all MHD modes are excited, including fast and slow modes. Since we include the compressible modes, we do not omit the cross-term in the magnetic energy, which for the general case is $\delta \mathbf{B} \cdot \mathbf{B}_0 \neq 0$. To leading order, the fluctuating part in the energy equation, when $|\delta \mathbf{B}| \ll |\mathbf{B}_0|$, will be (Federrath 2016)

$$\delta \epsilon_m \simeq \frac{\delta B B_0}{4\pi}. \quad (20)$$

Despite its simplicity, the accuracy of this model was proven to be remarkable when tested in numerical simulations of sub-Alfvénic turbulence (Federrath 2016; Beattie et al. 2020). We assume that turbulent kinetic energy is equal to magnetic energy fluctuations, hence

$$\frac{1}{2} \rho \delta v^2 = \frac{\delta B B_0}{4\pi} \quad (21)$$

As in DCF, we use the relation $\delta \theta = \delta B / B_0$, since the turbulent-to-ordered ratio is measured from the polarization angle distri-

bution. We obtain

$$B_0 = \sqrt{2\pi\rho} \frac{\delta v}{\sqrt{\delta\theta}}, \quad (22)$$

which can be solved for the Alfvén speed, $V_A = B_0 / \sqrt{4\pi\rho}$, as

$$V_A = \frac{1}{\sqrt{2}} \frac{\delta v}{\sqrt{\delta\theta}}. \quad (23)$$

As in DCF, we assume that there is a guiding field about which MHD waves propagate. We also assume that turbulent kinetic energy is equal to the fluctuating magnetic energy, *but we assume that $\delta B B_0$ is the dominant term in the magnetic energy, due to the compressible modes*. This term is neglected in previous methods, which rely on the assumption that turbulence is purely Alfvénic. The major difference between our equation and the DCF is that the $(\delta B/B_0)^n$ term in our equation appears with $n = -1/2$, while in DCF it is $n = -1$.

4.1. Testing the proposed method with 3D simulations

We apply the proposed method to the 3D compressible MHD simulations, see Section 2.2.2, in order to test its validity. We use the $\delta\theta$ and σ_v from Table 1. In the same Table we show in the V_A^{new} column the value computed using equation (23). It is evident that our model produces acceptably accurate estimates of the true V_A in all models.

The relative deviation of the estimated V_A from the true one is

$$\epsilon = \frac{|V_A^{true} - V_A^{est}|}{V_A^{true}}, \quad (24)$$

where V_A^{true} is the true V_A and V_A^{est} is the estimated value from the various methods. In Fig. 4 we show $\epsilon(\%)$ for all models. The black points correspond to DCF, blue to HH09, and red to the new proposed method (Eq. 23). DCF systematically overestimates the true value. HH09 produces very large estimates in the models with low M_s , while at higher M_s the method is more accurate. Our proposed method produces quite accurate values for the field strength independently of M_s . The mean deviation, ϵ , of our method is 17%. The largest deviation is seen in the model with $M_s = 4.0$, where $\epsilon = 27\%$.

The accuracy of our method does not depend on M_s . However our method systematically underestimates the true field strength. This can be explained by the non-homogeneity effect that we discussed in § 2.2.2. The polarization map includes dispersion due to density enhancements, hence $\delta\theta$ overestimates the $\delta B/B_0$ ratio. Only in the model with $M_s = 0.7$, where density inhomogeneities are minimal, the method slightly overestimates the field strength.

4.2. Limitations of our method

There are limitations of our method related to the observables and the physics behind the proposed equation.

1. Polarization angle maps are affected by density inhomogeneities, hence they do not probe the $\delta B/B_0$ term accurately. The observed spread is higher than the true ratio, hence the field strength is underestimated. This non-homogeneity effect is the dominant uncertainty in our method.

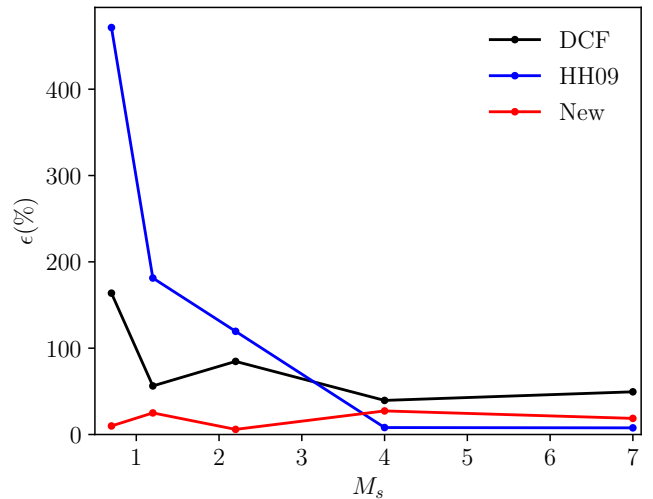


Fig. 4. Relative deviation of each method estimate for the different simulation models. All the models have $M_A = 0.7$.

2. As in DCF, we neglect the contribution of self-gravity. In the presence of self-gravity the field lines are bent and the observed $\delta\theta$ and δv are higher. Other methods have to be employed prior to ours, e.g. Girart et al. (2006) and Pattle et al. (2017), in order to remove the self-gravity effects from both polarization and spectroscopic maps.
3. Not all the MHD modes induce $\delta B/B_0$ variations. For example, for very strong fields, fast modes can propagate perpendicularly to the mean field and oscillate like an harmonica, without disturbing the field lines. These modes will contribute in velocity, but not in the polarization angle, biasing the magnetic field estimate to higher values. The tests we performed though show that this is not a very important effect.

5. Discussion & Conclusions

Dust polarization traces the magnetic field orientation in the POS, but not its strength. DCF and HH09 are the most widely applied methods that employ polarization data in order to estimate the strength of the field. They rely on the assumption that isotropic gas turbulent motions induce the propagation of small amplitude Alfvén waves, $|\delta B| \ll |B_0|$. Observations indicate that turbulence in the ISM is highly anisotropic, e.g. Higdon (1984) Heyer et al. (2008) and Planck Collaboration et al. (2016), see also § 2.2.3. The sufficiently high M_s in the ISM, e.g. (Heiles & Troland 2003), implies that compressible modes are important. Both DCF and HH09 neglect the compressible modes. As a result, the estimates of the magnetic field they provide may deviate significantly from the true value.

We tested the DCF method in synthetic observations from publicly available 3D MHD simulations. We found that DCF method systematically overestimates the true strength value. The previously reported reduction factor $f = 0.5$ is not supported by our analysis. We found similar results when we tested the HH09 method. However, the accuracy of the later improves significantly for models with high sound Mach numbers.

We proposed a new method to estimate the magnetic field strength in the ISM. We accounted for all MHD modes, both Alfvén and compressible. We assumed that: wave fluctuations are sufficiently small compared to the mean field strength,

$|\delta\mathbf{B}| \ll |\mathbf{B}_0|$; turbulent kinetic energy is equal to the fluctuating part of the magnetic energy density; the fluctuating magnetic energy is dominated by the $\delta B B_0$ cross-term, which represents the compressible modes. Instead of

$$B_0 = f \sqrt{4\pi\rho} \frac{\delta v}{\delta\theta}, \quad (25)$$

we proposed the following equation:

$$B_0 = \sqrt{2\pi\rho} \frac{\delta v}{\sqrt{\delta\theta}}, \quad (26)$$

where ρ is the gas density, δv is the spread in spectroscopic data emission lines and $\delta\theta$ is the dispersion of polarization angles.

We tested the validity of our equation in synthetic observations and we compared its accuracy to that of DCF and HH09. Although our proposed method does not guarantee an improvement of accuracy over HH09 for all sound Mach numbers, it does guarantee a uniformly low error independently of Mach number and without the need for a correction factor. This is a particularly attractive feature for cases where the Mach number is not known. For Mach numbers $\lesssim 3$ our method outperforms DCF and HH09 by large factors.

Acknowledgements. RS would like to thank J. Beattie for productive discussions and Dr. B. Burkhardt for her help with their numerical simulations. We thank A. Tritsis for his invaluable comments. We also thank N. D. Kylafis for his careful reading of the manuscript, V. Pavlidou and G. V. Panopoulou for fruitful discussions. (RS) would like to thank Dr. K. Christidis for his constant support during this project. This project has received funding from the European Research Council (ERC) under the European Unions Horizon 2020 research and innovation programme under grant agreement No. 771282.

Hull, C. L. H. & Zhang, Q. 2019, *Frontiers in Astronomy and Space Sciences*, 6, 3
 Kudoh, T. & Basu, S. 2003, *ApJ*, 595, 842
 Lazarian, A., Yuen, K. H., & Pogosyan, D. 2020, arXiv e-prints, arXiv:2002.07996
 Lee, H. M. & Draine, B. T. 1985, *ApJ*, 290, 211
 Lithwick, Y. & Goldreich, P. 2001, *ApJ*, 562, 279
 Maron, J. & Goldreich, P. 2001, *ApJ*, 554, 1175
 Miville-Deschénes, M. A., Levrier, F., & Falgarone, E. 2003, *ApJ*, 593, 831
 Montgomery, D., Brown, M. R., & Matthaeus, W. H. 1987, *J. Geophys. Res.*, 92, 282
 Montgomery, D. & Turner, L. 1981, *Physics of Fluids*, 24, 825
 Mouschovias, T. C., Tassis, K., & Kunz, M. W. 2006, *ApJ*, 646, 1043
 Myers, P. C. & Goodman, A. A. 1991, *ApJ*, 373, 509
 Ostriker, E. C., Stone, J. M., & Gammie, C. F. 2001, *ApJ*, 546, 980
 Oughton, S. & Matthaeus, W. H. 2020, *ApJ*, 897, 37
 Padoan, P., Goodman, A., Draine, B. T., et al. 2001, *ApJ*, 559, 1005
 Panopoulou, G., Tassis, K., Blinov, D., et al. 2015, *MNRAS*, 452, 715
 Panopoulou, G. V., Psaradaki, I., & Tassis, K. 2016, *MNRAS*, 462, 1517
 Pattle, K. & Fissel, L. 2019, *Frontiers in Astronomy and Space Sciences*, 6, 15
 Pattle, K., Ward-Thompson, D., Berry, D., et al. 2017, *ApJ*, 846, 122
 Pillai, T., Kauffmann, J., Tan, J. C., et al. 2015, *ApJ*, 799, 74
 Planck Collaboration, Ade, P. A. R., Aghanim, N., et al. 2016, *A&A*, 586, A138
 Portillo, S. K. N., Slepian, Z., Burkhardt, B., Kahraman, S., & Finkbeiner, D. P. 2018, *ApJ*, 862, 119
 Shebalin, J. V., Matthaeus, W. H., & Montgomery, D. 1983, *Journal of Plasma Physics*, 29, 525
 Soler, J. D., Alves, F., Boulanger, F., et al. 2016, *A&A*, 596, A93
 Soler, J. D., Hennebelle, P., Martin, P. G., et al. 2013, *ApJ*, 774, 128
 Sridhar, S. & Goldreich, P. 1994, *ApJ*, 432, 612
 Stephens, I. W., Looney, L. W., Dowell, C. D., Vaillancourt, J. E., & Tassis, K. 2011, *ApJ*, 728, 99
 Tang, Y.-W., Koch, P. M., Peretto, N., et al. 2019, *ApJ*, 878, 10
 Tritsis, A. & Tassis, K. 2016, *MNRAS*, 462, 3602
 Tritsis, A. & Tassis, K. 2018, *Science*, 360, 635
 Yoon, H. & Cho, J. 2019, *ApJ*, 880, 137
 Zweibel, E. G. 1990, *ApJ*, 362, 545

References

Andersson, B. G., Lazarian, A., & Vaillancourt, J. E. 2015, *ARA&A*, 53, 501
 Beattie, J. R. & Federrath, C. 2020, *MNRAS*, 492, 668
 Beattie, J. R., Federrath, C., & Seta, A. 2020, *MNRAS*[arXiv:2007.13937]
 Bialy, S. & Burkhardt, B. 2020, *ApJ*, 894, L2
 Burkhardt, B., Appel, S., Bialy, S., et al. 2020, arXiv e-prints, arXiv:2010.11227
 Burkhardt, B., Falceta-Gonçalves, D., Kowal, G., & Lazarian, A. 2009, *ApJ*, 693, 250
 Chandrasekhar, S. & Fermi, E. 1953, *ApJ*, 118, 113
 Cho, J. & Lazarian, A. 2002, *Phys. Rev. Lett.*, 88, 245001
 Cho, J. & Lazarian, A. 2003, *MNRAS*, 345, 325
 Cho, J. & Vishniac, E. T. 2000, *ApJ*, 538, 217
 Cho, J. & Yoo, H. 2016, *ApJ*, 821, 21
 Chuss, D. T., Andersson, B. G., Bally, J., et al. 2019, *ApJ*, 872, 187
 Clark, S. E., Peek, J. E. G., & Putman, M. E. 2014, *ApJ*, 789, 82
 Cox, N. L. J., Arzoumanian, D., André, P., et al. 2016, *A&A*, 590, A110
 Davis, L. 1951, *Phys. Rev.*, 81, 890
 Falceta-Gonçalves, D., Lazarian, A., & Kowal, G. 2008, *ApJ*, 679, 537
 Federrath, C. 2016, *Journal of Plasma Physics*, 82, 535820601
 Franco, G. A. P. & Alves, F. O. 2015, *ApJ*, 807, 5
 Franco, G. A. P., Alves, F. O., & Girart, J. M. 2010, *ApJ*, 723, 146
 Girart, J. M., Rao, R., & Marrone, D. P. 2006, *Science*, 313, 812
 Goldreich, P. & Sridhar, S. 1995, *ApJ*, 438, 763
 Goldreich, P. & Sridhar, S. 1997, *ApJ*, 485, 680
 Goldsmith, P. F., Heyer, M., Narayanan, G., et al. 2008, *ApJ*, 680, 428
 Heiles, C. & Troland, T. H. 2003, *ApJS*, 145, 329
 Heitsch, F., Zweibel, E. G., Mac Low, M.-M., Li, P., & Norman, M. L. 2001, *ApJ*, 561, 800
 Hensley, B. S., Zhang, C., & Bock, J. J. 2019, *ApJ*, 887, 159
 Heyer, M., Gong, H., Ostriker, E., & Brunt, C. 2008, *ApJ*, 680, 420
 Heyvaerts, J. & Priest, E. R. 1983, *A&A*, 117, 220
 Higdon, J. C. 1984, *ApJ*, 285, 109
 Hildebrand, R. H., Kirby, L., Dotson, J. L., Houde, M., & Vaillancourt, J. E. 2009, *ApJ*, 696, 567
 Hill, A. S., Benjamin, R. A., Kowal, G., et al. 2008, *ApJ*, 686, 363
 Hoq, S., Clemens, D. P., Guzmán, A. E., & Cashman, L. R. 2017, *ApJ*, 836, 199
 Houde, M., Vaillancourt, J. E., Hildebrand, R. H., Chitsazzadeh, S., & Kirby, L. 2009, *ApJ*, 706, 1504

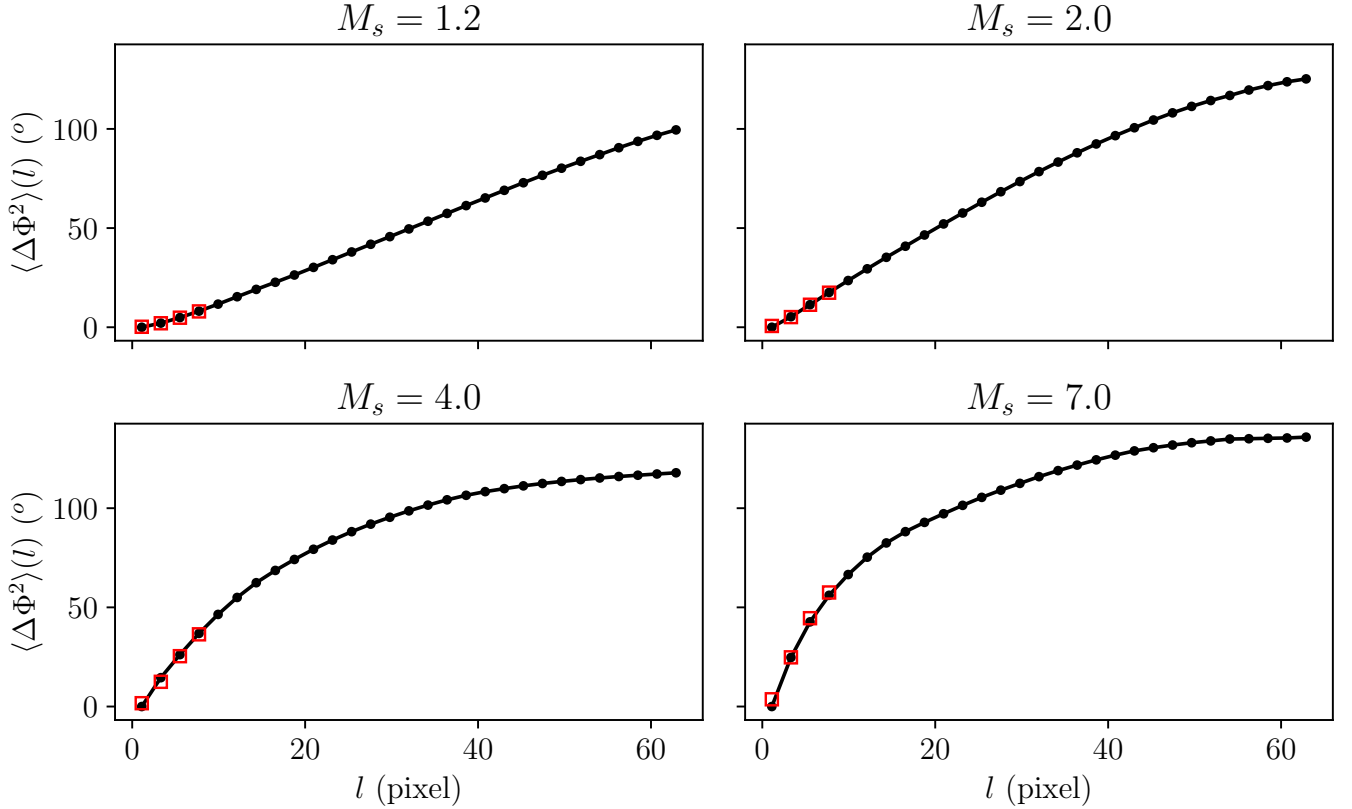


Fig. 1. Structure functions for the different simulation setups. Red circles show the best fit values.

Table A.1. Structure function fits with varying fitting range.

Points	l_{max} (pixels)	$\sqrt{\langle B_t^2 \rangle}/B_0$	V_A^{HH09} (km/s)
4	7.7	0.088	5.2
10	20.9	0.109	4.2
15	32.0	0.131	3.5
20	43.0	0.150	3.1
26	56.3	0.165	2.8

Notes. $\sqrt{\langle B_t^2 \rangle}/B_0$ is measured in radians.

Table A.2. Fitting parameters of the HH09 method.

M_s	b (°)	m	l (pixels)
0.7	1.54	0.19	4.7
1.2	2.10	0.27	4.1
2.2	3.19	0.37	3.5
4.0	4.46	0.54	2.7
7.0	6.24	0.54	2.7

Notes. These fits have been produced using four points in the structure function. The m parameter is dimensionless.

Appendix A: Structure function fitting

We examine how the number of points used in the fit of the structure function affects the estimation of the magnetic field strength. For the simulation model with $M_s = 0.7$ we produce different fits by varying the number of points used. In Table A.1 we show in the first column the total number of points used for the fit. The column l_{max} shows the maximum scale of the fitting range and in the $\langle B_t^2 \rangle^{1/2}/B_0$ column we show the derived ratio from each fit. In the column V_A^{HH09} we show the estimated field strength using equation (17). The turbulent velocity of the model with $M_s = 0.7$ is $\sigma_v = 0.46$ km/s, see Table 1. The estimated strength value decreases as we use more points in the fit. This demonstrates the dependence of the estimated values, V_A^{HH09} , on the fitting range of the structure function. We experimented with the fits of the other simulation models, $M_s = 1.2 - 7.0$. Not all of them were so sensitive to the number of points used.

In Table A.2 we present the structure function fitting parameters for each simulation model when only four points are used. The $\langle B_t^2 \rangle^{1/2}/B_0$ values in Table 1 correspond to these fittings. In Fig. 1 we show, similar to Fig. 3, the structure function plots for the models with $M_s = 1.2 - 7.0$.